Efficient H$_2$O$_2$ photocatalysis by a novel organic semiconductor with electron donor-acceptor interface

Rong Ji [a], Yuming Dong [a,*], Xinyu Sun [a], Chengsi Pan [a], Yunfan Yang [a], Hui Zhao [a], Yongfa Zhu [a,b]

[a] *International Joint Research Center for Photo-Responsive Molecules and Materials, School of Chemical and Material Engineering, Jiangnan University, Wuxi 214122, China*
[b] *Department of Chemistry, Tsinghua University, Beijing 100084, China*

A B S T R A C T

Nowadays, considerable attention has been directed towards the two-electron oxygen reduction for the photocatalytic H$_2$O$_2$ production. However, the challenge of insufficient charge separation capacity markedly constrains the rate of H$_2$O$_2$ production. Herein, we designed a donor-acceptor (D-A) interface characterized by rapid charge migration and separation to enhance the photocatalytic H$_2$O$_2$ production. Specifically, naphthalenetetracarboxylic acid-diaminotriazole as an organic molecule has been judiciously chosen as the electron donor, while perylenetetracarboxylic acid serves as the electron acceptor. The novel semiconductor with D-A interface performs markedly strong internal electric field and demonstrates an excellent H$_2$O$_2$ production rate of 3176 μM h^{-1}. The pronounced internal electric field facilitated by the D-A interface effectively expedites charge separation and induces the migration of photogenerated carriers to the O$_2$ reduction sites. This study introduces a novel paradigm for the design of D-A interfacial organic materials aimed at realizing enhanced photocatalytic capabilities.

1. Introduction

Hydrogen peroxide (H$_2$O$_2$) has been recognized as one of the most valuable commodity chemicals with broad attention. Recently, the conventional methods of H$_2$O$_2$ production still suffer from various problems such as high energy consumption, serious pollution, and low selectivity [1]. Thus, the preparation of H$_2$O$_2$ by solar energy through semiconductor photocatalysts is a clean and environmental-friendly approach [2,3]. Especially, photocatalytic two-electron (2e$^-$) oxygen reduction (ORR) technology has become the most attractive technology to H$_2$O$_2$ production due to its green and sustainable characteristics [4,5]. However, rapid photogenerated carrier recombination behaviors result in poor photocatalytic H$_2$O$_2$ production activity for these photocatalysts. Therefore, overcoming the above drawbacks is the key to improve the efficiency of photocatalytic H$_2$O$_2$ production.

In particular, various conjugated organic materials are favored in photocatalytic field due to their excellent broad-spectrum absorption and structural adjustability[6–9]. Recently, several conjugated organic materials have been developed by our group [10–13]. However, most of the organic photocatalysts still face the problem of slow photogenerated carrier separation, which limits the rate of their H$_2$O$_2$ production. To

date, many strategies have been proposed to accelerate the charge separation of organic semiconductor. For instance, morphological design and molecular doping display enhanced photocatalytic H$_2$O$_2$ production activity due to the effectively improved intramolecularly charge transfer [14–16]. Unfortunately, by the above intramolecular improvement, the photogenerated electrons of organic semiconductor tend to recombine. And photogenerated carriers cannot arrive the surface to participate in the reaction, suppressing the rate of H$_2$O$_2$ production. Therefore, exploring novel and effective ways is necessary to enhance interlayer charge transfer of organic photocatalysts, which is crucial to realize the breakthrough performance in photocatalytic H$_2$O$_2$ production.

Inspired by the electron-donor properties of naphthalenetetracarboxylic acid-diaminotriazole (N-AT) organic molecule and electron-acceptor properties of perylene-based materials, forming an interface with electron donor-acceptor (D-A) feature has come up. To our knowledge, as a nitrogen-rich heterocycle molecule, the N-AT molecule can potentially form multiple hydrogen bonds for further self-assembly to form two-dimensional (2D) nanosheets. Meanwhile, perylene-based materials have drawn great interest due to the extensive light absorption and π-π stacking electron migration [10]. Herein, N-AT

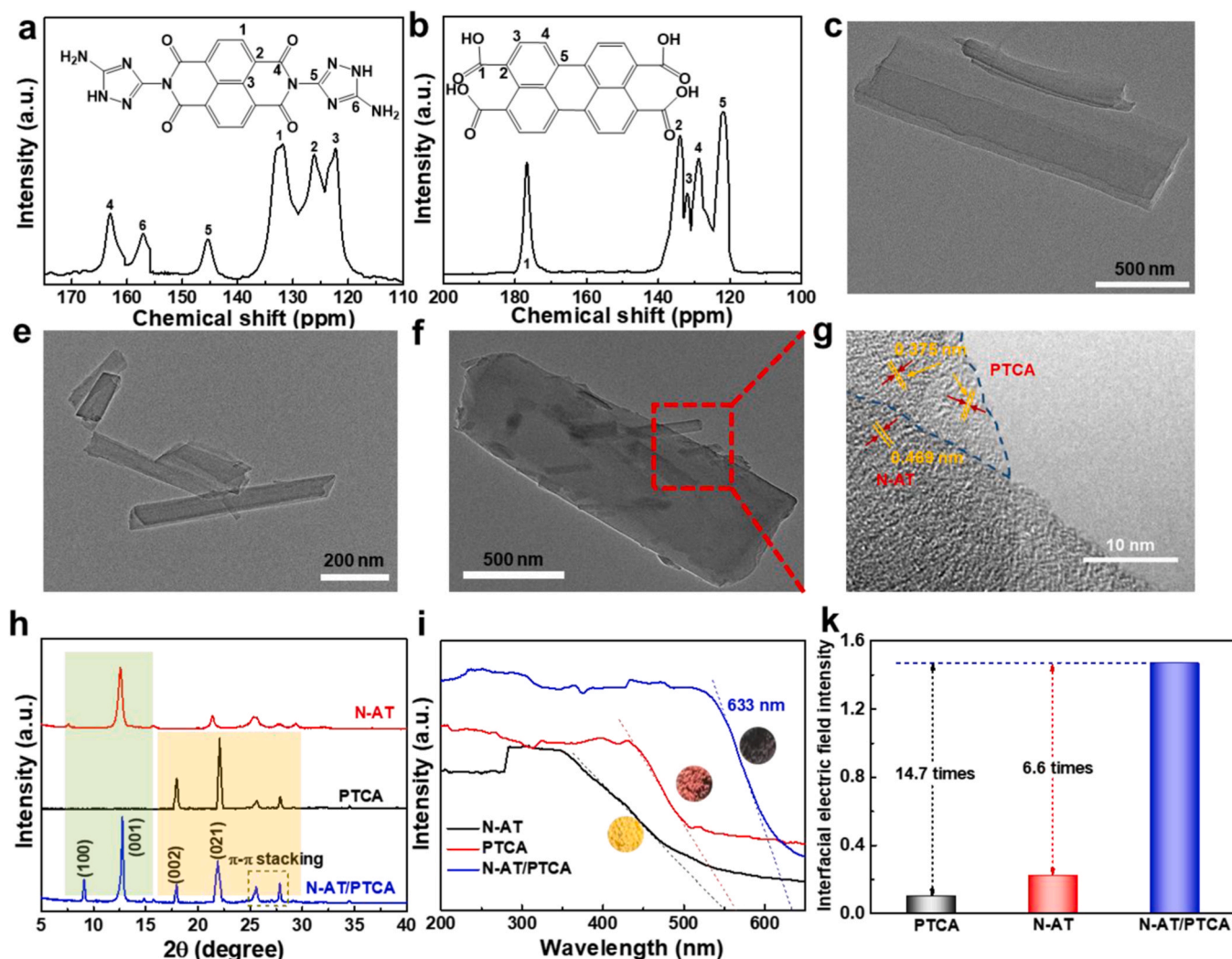**Fig. 1.** (a-b) Solid-state ^{13}C NMR spectra of N-AT and PTCA. (c-f) TEM images of N-AT, PTCA and N-AT/PTCA. (g) HRTEM image of N-AT/PTCA. (h) the interfacial electric field intensity. (i) XRD, (k) UV–vis DRS of N-AT, PTCA and N-AT/PTCA.

is chosen as electron donor which is used to polymerize the electron-acceptor monomer of perylene- tetracarboxylic acid (PTCA) in this work. It has been proved that the interface with D-A feature between N-AT and PTCA can build a charge transport channel, which dramatically accelerates spatial charge separation. The giant interfacial electric field at the interface greatly provides driving force for charge separation to accelerate electron transfer. Moreover, O_2 can be adsorbed at the place of charge enrichment. And the separated electrons are urged reacting with O_2 to prepare H_2O_2 quickly. Therefore, N-AT/PTCA shows excellent photocatalytic performance for the H_2O_2 production (3176 μM h^{-1}).

2. Materials and methods

2.1. Chemicals and reagents

3,5-diamino-1 H-1,2,4-triazole (DAT), 1,4,5,8-naphthalenetetracarboxylic dianhydride (NTCDA) and 3, 4, 9, 10-perylenetetracarboxylic dianhydride (PTCDA) were purchased from Aladdin Reagent. Dimethylacetamide (DMAc), N-methyl pyrrolidone (NMP) and dimethylformamide (DMF) were obtained from Sinopharm Chemical Reagent Co., Ltd. All chemical reagents and materials were used as received without further purification.

2.2. Photocatalyst preparation

First, 99.1 mg DAT was dissolved in 10 mL (DMAc) under N_2 condition in an ice bath. And then 134 mg of NTCDA was added into the above solution and stirred for 1 h. Subsequently, 25 mL of DMAc was mixed in the solution. Finally, the reaction solution was transferred into a 50 mL Teflon-lined autoclave and heated in an electric oven at 180 °C for 12 h [17]. The product was washed several times with dimethylformamide (DMF), methanol and distilled water. The collected solid was obtained through filtration freeze-dried. The sample was marked as N-AT. Then, 0.1 g PTCDA was dissolved in the 15 mL NMP solution, which was hydrolyzed into PTCA [18]. And the appropriate amount of N-AT was redispersed in 20 mL NMP solution and subsequently added into the above solution and stirred for 1 h. The above solution was heated at 180 ºC for 24 h in a preheated oven (Scheme S1). The obtained products were collected and centrifuged with NMP, ethanol, and hot water for three times, and marked as N-AT/PTCA-X ("X" is the mass ratio of N-AT relative to PTCA, namely, 0.2:1, 0.5:1, 1:1, 2:1. Besides, N-AT/PTCA-1:1 was chosen for analysis, which performed the best photocatalytic activity). The self-assembly PTCA was obtained without adding N-AT.
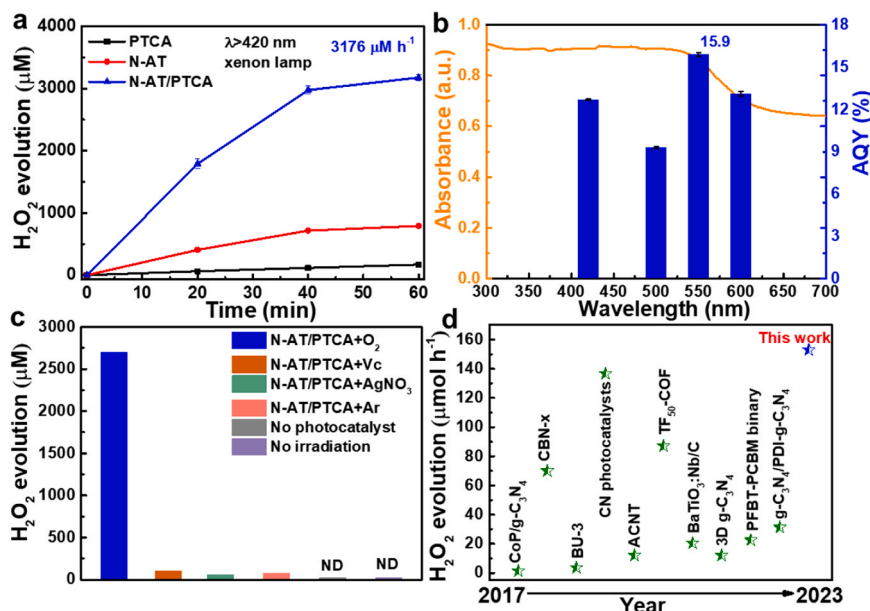
Fig. 2. (a) Time profiles of H_2O_2 production for prepared samples. (b) overlayer of apparent quantum yield (AQY) and UV–vis absorption. (c) photocatalytic H_2O_2 production activity of N-AT/PTCA under different conditions (ND means not detected). (d) photocatalytic H_2O_2 production rates from recently reported photo-catalysts. (solution: 50 mL aqueous solution containing 10 vol% ethanol; O_2 bubbling; light source: Xe lamp with a $\lambda > 420$ nm filter; catalyst: 1 g L^{-1}. Error bars on three independent H_2O_2 production tests).

2.3. Photocatalyst characterization

The phase structures of as-prepared photocatalysts were measured by a D8 X-ray diffraction (XRD) at 5–50° with a scanning step of 5°/min (AXS, Bruker). The chemical structures of as-prepared samples were analyzed by the solid-state ^{13}C NMR information (Bruker, 400 MHz). The surface functional groups were studied Fourier-transform infrared (FT-IR, Nicolet iS5, Thermofisher) and X-ray photoelectron spectroscopy (XPS, Thermo Scientific K-Alpha$^+$, Thermofisher). The microstructures were tested by high-resolution transmission electron microscopy (HRTEM, JEM-2100 plus JEOL). The surface potential of given materials was recorded by Kelvin probe force microscopy (KPFM, SPM-9700HT, Shimadzu). The diffuse reflectance absorption spectra (DRS) of as-obtained samples were analyzed on a UV–vis spectrophotometer (UV-3600, Shimadzu). The steady-state photoluminescence (PL) spectroscopy was analyzed by the FS5 (Edinburgh) with an excitation wavelength of 375 nm. Photoluminescence decay spectra was recorded on a LifeSpec II fluorescence lifetime spectrometer (Edinburgh). Rotating disk electrode (RDE) measurements was performed by a glassy carbon rotating disk electrode (RRDE- E6R1, PINE). The electron paramagnetic resonance (EPR) signals were detected by the EMXplus-6/1 (Bruker). The detailed characterizations of the as prepared samples, the details of theoretical calculations and other experimental section were supplemented in the Supplementary Material.

3. Results and discussion

3.1. Construction of D-A Interface between N-AT and PTCA

First, the molecular structure of N-AT and PTCA is subsequently confirmed by a range of spectroscopic characterizations. Solid-state ^{13}C nuclear magnetic resonance (^{13}C NMR) shows the signature peaks from 1,4,5,8-naphthalenetetracarboxylic dianhydride (NTCDA) (122 ppm, 126 ppm, 132 ppm and 163 ppm) and diaminotriazole (DAT) (157 ppm and 145 ppm) moieties (Fig. 1a) [17]. Meanwhile, the carbon on the carbonyl group appears in the lowest field with a chemical shift of 177 ppm. Due to the conjugation effect, the chemical shift of the edge carbon of perylene nucleus was 134 ppm. And the chemical shifts are

122–132 ppm because of the in-discriminability of the conjugations of perylene rings (Fig. 1b) [19]. In addition, Fourier transform infrared (FT-IR) spectrum (Fig.S1a) exhibits a peak at 1248 cm^{-1} that can be assigned to the C-O stretching vibration of PTCA [20]. And the C=O stretching vibration of PTCA is located at 1692 cm^{-1}. The peak at 1355 cm^{-1} belongs to the C-N stretching vibration [21]. Together with the disappearance of the C-O stretching vibration at 1248 cm^{-1}, which clearly indicates the formation N-AT from the reaction between DAT and NTCDA [22]. The characteristic signal at 3346 cm^{-1} to the N-H stretching vibration is still preserved in N-AT [17]. Moreover, the surface electronic structure of N-AT/PTCA is also detected (Fig.S1b) [22–25]. The transmission electron microscopy (TEM) image exhibits that the N-AT consists of two-dimensional (2D) nanosheets (Fig. 1c). And the TEM demonstrates that PTCA owns stacked nanosheets with abundant overlapping areas (Fig. 1e). Furthermore, the thickness information of N-AT and PTCA nanosheets are observed (Fig.S2). Thus, the above analysis proves that the molecules of N-AT and PTCA are successfully prepared. As shown in Fig. 1 f, the N-AT/PTCA sample is successfully constructed via π-π stacking by self-assembly process. High-resolution transmission electron microscopy (HRTEM) of Fig. 1 g reveals that N-AT/PTCA has formed D-A interface, in which d-spacing of 0.375 and 0.469 nm assigned to PTCA and N-AT, respectively. In order to explain the molecular topology, all samples are analyzed by X-ray diffraction (XRD) as shown in Fig. 1 h. The lattice fringes observed in N-AT/PTCA correspond to the (100) and (001) crystal planes of N-AT, while the crystal plane signals of (002) and (021) assign to PTCA [18]. Moreover, continuous peaks at $2\theta = 25.4°$ and $27.8°$ can be belong to the strong π-π stacking between N-AT and PTCA [26].

Besides, the optical properties and band structure of all samples are examined by UV–vis DRS and Mott-Schottky plots. Fig. 1i exhibits that N-AT/PTCA has the longest absorption wavelength even up to 633 nm compared with pure N-AT and PTCA. Accordingly, the bandgaps of N-AT (2.33 eV) and PTCA (2.31 eV) are calculated by Kubelka-Munk function (Fig.S3). Mott-Schottky plots (Fig. S4) show that all prepared samples exhibit n-type semiconductor properties (positive slope). The flat band positions derived from the intersection are −1.05 and −0.85 V, which is approximately equal to the conduction band (CB) edge of N-AT and PTCA respectively [4]. The valence band (VB) potentials of N-AT and
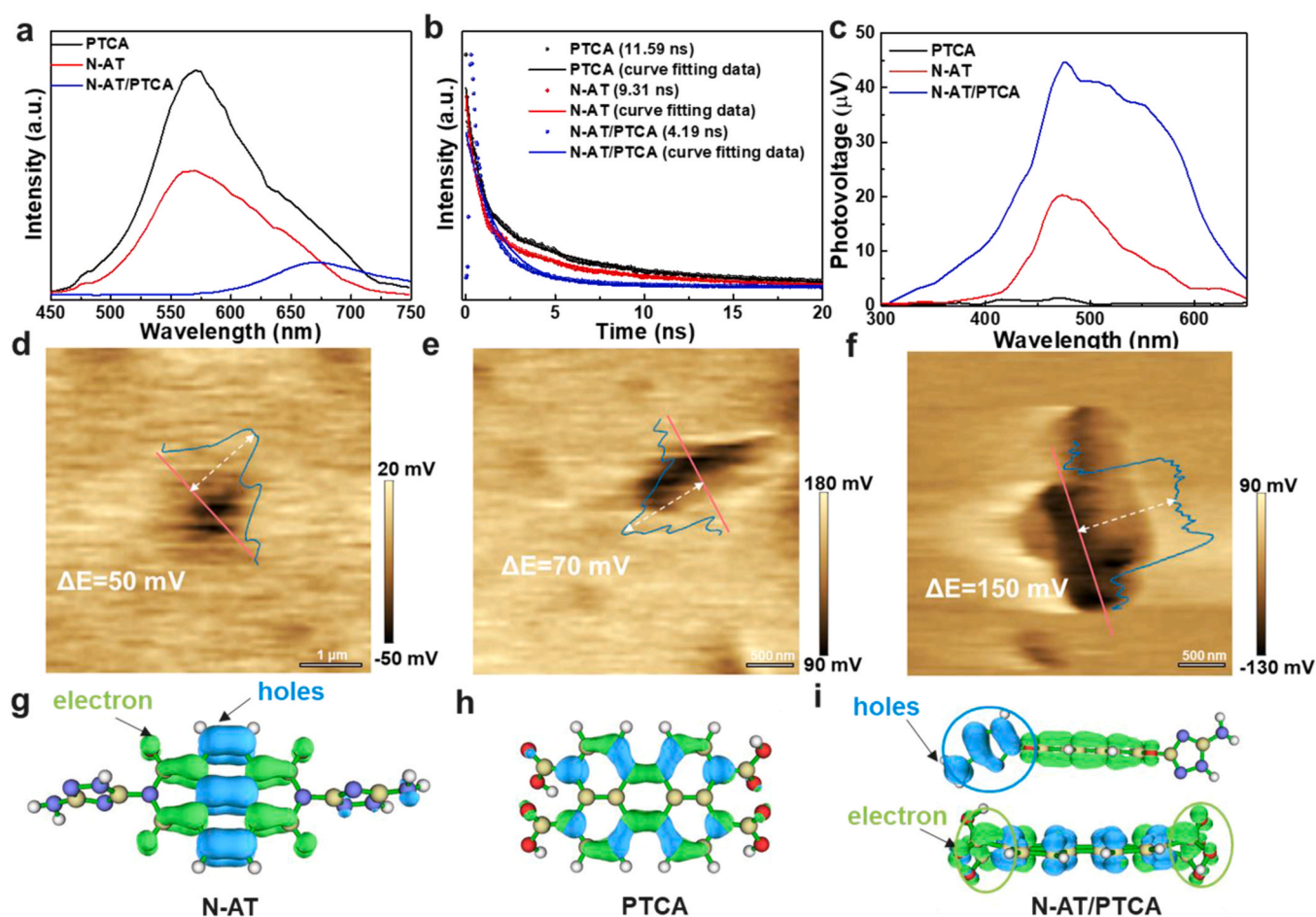
Fig. 3. (a) steady-state PL spectra, (b) transient-state PL spectra and (c) surface photovoltage spectra of all prepared samples. (d-f) surface potential and (g-h) electron-hole distribution in excited states of N-AT, PTCA and N-AT/PTCA.

PTCA are calculated to 1.28 V and 1.46 V, respectively (Fig. S5). The electrostatic potential (ESP) distributions of N-AT and PTCA also explain that the D-A interface can

facilitate the separation and transportation of the charge carriers (Fig. S6). According to the theoretical results, the lowest unoccupied molecular orbitals (LUMO) and the highest occupied molecular orbitals (HOMO) of N-AT and PTCA are mainly located in delocalized π electrons (Fig. S7) [27–31], which are primarily responsible for the interaction between N-AT and PTCA. Combined with the above analysis of CB, it can be found that the CB of N-AT is lower than that of PTCA before contact. When N-AT and PTCA are in close contact, electrons are transferred spontaneously from N-AT to PTCA through the interface. Thus, an IEF in the direction from N-AT to PTCA generated at the interface. The result of theoretical calculations demonstrates that LUMO and HOMO of N-AT/PTCA at the interface are respectively lied on the PTCA and N-AT (Fig. S8), which reveals that N-AT owns outstanding electron-donor properties and PTCA has electron-acceptor properties (D-A feature) [32,33].

Based on the above results, the novel self-assembly N-AT/PTCA organic semiconductor with D-A interface has been successfully designed via π-π stacking interaction for photocatalytic H_2O_2 production. Furthermore, the internal electric field of all samples is evaluated through photo-generated charge density surface voltages and open circuit potentials (OCP, Fig. S9a-b). According to Le Formal and Gratzel et al., the internal electric field is proportional to the number of charges accumulated at the surface, by integrating the measured transient photocurrent density minus the steady-state values of photocurrent with respect to time [34–36]. Thus, as shown in Fig. 1k, N-AT/PTCA performs

the obvious strongest IEF is 14.7 and 6.6 times that of pure PTCA and N-AT, respectively. As a consequence, N-AT/PTCA possesses giant interfacial electric field at the interface, which dramatically accelerating photo-generated electrons to join in the O_2 reduction reaction. Therefore, N-AT/PTCA exhibits a much-enhanced rate of H_2O_2 production.

3.2. D-A interface of N-AT/PTCA enhanced photocatalytic H_2O_2 production

The photocatalytic H_2O_2 production experiments of all prepared samples are carried out using ethanol as a sacrificial agent under visible-light (λ>420 nm) irradiation. The detailed supplementary information about photocatalytic properties is also observed (Fig. S10-12). Noticeably, the highest H_2O_2 production rate of the coassembly N-AT/PTCA arrives up to 3176 M h^{-1} (Fig. 2a), which is 4.1 and 16.7 times as that of pure N-AT and PTCA, respectively. Moreover, the rate of H_2O_2 production without any sacrificial agent is 505 µM h^{-1} (Fig. S13b). Interestingly, the activity of H_2O_2 production is positively associated with internal electric field (IEF). Under visible light, the H_2O_2 production ability can be maintained for more than 6 cycles (Fig. S14a) without significantly decrease, and the continuous H_2O_2 production for more than 8 h (Fig. S14b). Particularly, there is no obvious change in the XRD and FT-IR of N-AT/PTCA after long-time photocatalytic reaction (Fig. S15). Intriguingly, the N-AT/PTCA photocatalyst exhibits lower decomposition rate which is beneficial for H_2O_2 accumulation (Fig. S16).

In addition, the wavelength-dependent H_2O_2 yield and apparent quantum yield (AQY) of N-AT/PTCA are conducted by using different
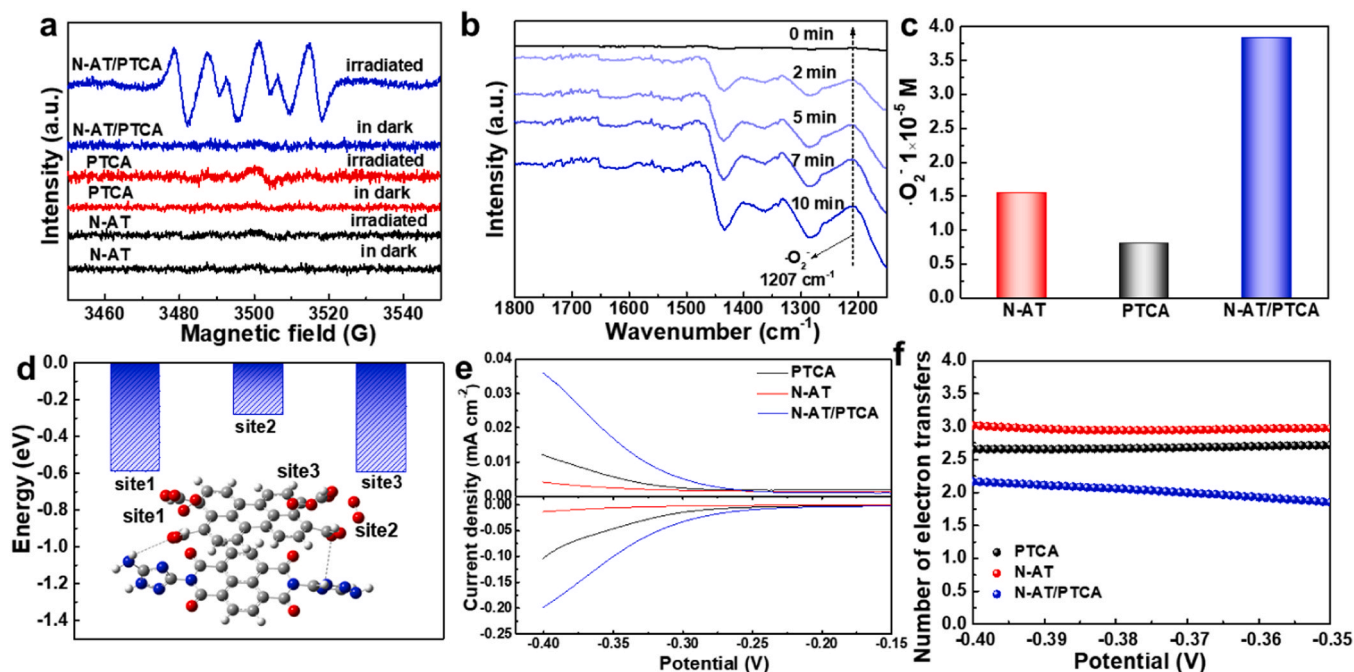
Fig. 4. (a) EPR spectra of DMPO-·O$_2^-$. (b) in situ DRIFT spectra of N-AT/PTCA recorded during photocatalytic H$_2$O$_2$ evolution. (c) Photocatalytic yield of ·O$_2^-$ detected by NBT method of all prepared samples. (d) The RRDE polarization curve over all prepared samples coated electrodes at sample rotation rate (ω=1600 rpm) at room temperature. The ring current (top) and disc current (bottom). (f) the corresponding number (n) of electron transfer as a function of the applied potential. The electrochemical measurements are performed in phosphate buffer solution (0.1 M pH = 6.9) with a scan rate of 10 mV s^{-1} in O$_2$ saturated electrolyte at 1600 rpm.

bandpass filters (Fig. 2b, Fig. S17). The result is consistent with the absorption spectra, indicating that the photoactivity is positively correlated with light absorption. The maximum AQY (15.9%) are produced at 550 nm, which is due to the good electronic excitation at 550 nm. It is worth noting that when AgNO$_3$ is added to capture electrons and Vitamin C (Vc) is added to capture ·O$_2^-$, almost no H$_2$O$_2$ is produced (Fig. 2c), indicating that H$_2$O$_2$ is mainly generated from ORR. Notably, no H$_2$O$_2$ is detected in the dark or in the absence of a catalyst, which means that the formation of H$_2$O$_2$ is a photocatalytic process. As shown in Fig. 2d, the H$_2$O$_2$ production rate of N-AT/PTCA is higher than that of other previously reported photocatalysts to date (Table S1). Considering the excellent performance of N-AT/PTCA for H$_2$O$_2$ production, it is urgent to study the key scientific problems orienting the photocatalytic performance.

3.3. D-A interface of N-AT/PTCA enhanced high-efficiency charge separation

The superior photocatalytic H$_2$O$_2$ production performance comes from efficient electron-hole separation. As a dynamic factor, the interfacial electric field (IEF) not only drives charge separation but also affects the direction of charge transfer. As shown in Fig. 3a, the steady-state photoluminescence (PL) intensity of N-AT/PTCA is significantly lower compared with that of pure N-AT and PTCA, manifesting that IEF promote photoinduced electron transfer. Besides, the carrier lifetime (4.19 ns) of N-AT/PTCA detected by transient-state PL is shorter than that of other photocatalysts due to the rapid charge migration (Fig. 3b) [37,38]. The arc radius of EIS can be used to determine the resistance of charge transfer. The arc radius of N-AT/PTCA is much smaller compared to N-AT and PTCA (Fig. S19), which suggests that coassembly N-AT/PTCA favors charge transfer[39]. The surface photovoltage (SPV) also confirms the faster carrier transfer. As shown in Fig. 3c, N-AT/PTCA exhibits a stronger SPV signal, revealing more efficient charge separation [40]. Furthermore, the Kelvin probe force microscopy (KPFM) is shown in Fig. 3d-e. Obviously, the surface potential of N-AT/PTCA (Δ E=150 mV) is much higher than that of N-AT (Δ E=50 mV) and PTCA

(Δ E=70 mV). And the absolute values of Zeta potential (Fig. S20) of N-AT/PTCA (-27.3 mV) is much higher than N-AT (17.0 mV) and PTCA (10.7 mV). The above results further confirm again that the N-AT/PTCA exists the strong interfacial electric field (IEF) at the D-A interface [41]. In addition, N-AT/PTCA possesses more allowed transition states, which also has a higher orbital contribution to the excited states (Fig. 3i). This result verifies that the photogenerated electrons of N-AT can transit directly to PTCA more easily, then promoting the O$_2$ reduction for H$_2$O$_2$ production.

3.4. Mechanism for enhanced photocatalytic H$_2$O$_2$ production

Due to the advantage of D-A interface promoting charge transfer, the mechanism for photocatalytic H$_2$O$_2$ production by electrons migrating to the active sites is also worth researching. In order to identify the species of reactive oxygen species in the ORR process, electron paramagnetic resonance (EPR) spectroscopy (DMPO) is carried out with 5,5-dimethyl-1-pyrroline N-oxide as a spin trapping agent under light and dark conditions, respectively. As a result, the typical six characteristic signals of DMPO-·O$_2^-$ is clearly observed in N-AT/PTCA under light irradiation (Fig. 4a), while that is absent in the dark, meaning the generation of ·OOH intermediate species. In contrast, the signal of DMPO-·O$_2^-$ by pure N-AT and PTCA is not found in either light or dark. As displayed in Fig. 4b, the signal strength at 1207 cm^{-1} attributed to ·O$_2^-$ gradually increases together with the enhancement of illumination time for the N-AT/PTCA photocatalytic system, which affirms the formation of ·OOH intermediate species and the two-step single electron route [42–44]. Different from N-AT/PTCA, the in situ DRIFT spectra of N-AT and PTCA under photoirradiation has no obvious change at the corresponding characteristic peak position, which is difficult to detect due to a small amount of H$_2$O$_2$ (Fig. S21). Meanwhile, the production of ·O$_2^-$ within N-AT/PTCA under photocatalytic conditions is confirmed and quantified by the characteristic reaction with nitro blue tetrazolium (NBT) (Fig. 4c) [45]. The photocatalytic yield of ·O$_2^-$ by SA-NDI detected by NBT method is 3.8×10^{-5} M, significantly higher than that of N-AT (1.5×10^{-5} M) and PTCA (0.8×10^{-5} M), demonstrating the D-A

interface facilitates the formation of ·OOH intermediates (Fig. 4b). For N-AT/PTCA photocatalyst, the adsorption energy (E_{ads}) of O_2 at PTCA (electron-acceptor) is more obvious, which means that the D-A interface can dramatically increase the adsorption capacity of O_2 (Fig. 4d, Table S2) [46–48].

The selectivity of producing H_2O_2 in O_2 saturated phosphate buffer solution electrolyte (0.1 M pH=6.9) is studied using rotating ring disk electrode (RRDE). The RRDE polarization curves on all prepared samples coated electrodes are measured at 1600 rpm (Fig. 4e). The reduction disk current (I_d) of N-AT/PTCA becomes stronger compared with pure N-AT and PTCA. Due to the rapid diffusion of more H_2O_2 generated by the disk part to the ring part, the positive oxide ring current (I_r) is enhanced [40]. In addition, the average number (n) of electron transfer in the oxygen reduction reaction is measured (Fig. 4f). The n values of N-AT, PTCA and N-AT/PTCA are 3.0, 2.7 and 2.0 (1.2 V vs RHE, 1600 rpm), respectively. Therefore, the H_2O_2 production by N-AT/PTCA through 2e$^-$ ORR is the main ORR pathway.

4. Conclusion

A new type of organic semiconductor with D-A interface has been successfully prepared and used for efficient photocatalytic H_2O_2 production. The D-A interface between N-AT and PTCA is conducive to the formation of a giant interfacial electric field for accelerating charge separation and transfer. The DFT calculation results show that the D-A interface urges photogenerated electrons to migrate to the O_2 adsorption site, which is beneficial for H_2O_2 production by 2e$^-$ O_2 reduction reaction. Therefore, N-AT/PTCA displays an efficient H_2O_2 production rate of 3176 μM h^{-1} and an AQY of 15.9% at 550 nm. This paper provides a new idea for the design of organic materials with D-A interface to achieve efficient H_2O_2 production.

CRediT authorship contribution statement

Yongfa Zhu: Funding acquisition. **Xinyu Sun:** Methodology. **Yuming Dong:** Writing – original draft, Supervision, Funding acquisition, Conceptualization. **Rong Ji:** Writing – review & editing, Writing – original draft, Investigation, Formal analysis, Conceptualization. **Yunfan Yang:** Writing – review & editing. **Chengsi Pan:** Supervision. **Hui Zhao:** Supervision.

Declaration of Competing Interest

The authors declare that they have no known competing financial interests or personal relationships that could have appeared to influence the work reported in this paper.

Data availability

Data will be made available on request.

Appendix A. Supporting information

Supplementary data associated with this article can be found in the online version at doi:10.1016/j.apcatb.2024.123884.

References

[1] X. Zhang, P. Ma, C. Wang, L. Gan, X. Chen, P. Zhang, Y. Wang, H. Li, L. Wang, X. Zhou, K. Zheng, Unraveling the dual defect sites in graphite carbon nitride for ultra-high photocatalytic H_2O_2 evolution, Energy Environ. Sci. 15 (2022) 830–842.

[2] S. Wang, Z. Xie, D. Zhu, S. Fu, Y. Wu, H. Yu, C. Lu, P. Zhou, M. Bonn, H. Wang, Q. Liao, H. Xu, X. Chen, C. Gu, Efficient photocatalytic production of hydrogen peroxide using dispersible and photoactive porous polymers, Nat. Commun. 14 (2023) 6891.

[3] X. Wang, X. Yang, C. Zhao, Y. Pi, X. Li, Z. Jia, S. Zhou, J. Zhao, L. Wu, J. Liu, Ambient preparation of benzoxazine-based phenolic resins enables long-term sustainable photosynthesis of hydrogen peroxide, Angew. Chem. Int. Ed. 62 (2023). Articl e202302829.

[4] H. Che, X. Gao, J. Chen, J. Hou, Y. Ao, P. Wang, Iodide-Induced fragmentation of polymerized hydrophilic carbon nitride for high-performance quasi-homogeneous photocatalytic H_2O_2 production, Angew. Chem. Int. Ed. 60 (2021) 25546–25550.

[5] Y. Zhang, C. Pan, G. Bian, J. Xu, Y. Dong, Y. Zhang, Y. Lou, W. Liu, Y. Zhu, H_2O_2 generation from O_2 and H_2O on a near-infrared absorbing porphyrin supramolecular photocatalyst, Nat. Energy 8 (2023) 361–371.

[6] C. Wu, Z. Teng, C. Yang, F. Chen, H.B. Yang, L. Wang, H. Xu, B. Liu, G. Zheng, Q. Han, Polarization engineering of covalent triazine frameworks for highly efficient photosynthesis of hydrogen peroxide from molecular oxygen and water, Adv. Mater. 34 (2022) 2110266.

[7] Z. Yong, T. Ma, Solar-to-H_2O_2 catalyzed by covalent organic frameworks, Angew. Chem. Int. Ed. 62 (2023) e202308980.

[8] D. Tan, R. Zhuang, R. Chen, M. Ban, W. Feng, F. Xu, X. Chen, Q. Wang, Covalent organic frameworks enable sustainable solar to hydrogen peroxide, Adv. Funct. Mater. (2023) 2311655..

[9] S. Chai, X. Chen, X. Zhang, Y. Fang, R.S. Sprick, X. Chen, Rational design of covalent organic frameworks for efficient photocatalytic hydrogen peroxide production, Environ. Sci. Nano 9 (2022) 2464–2469.

[10] J. Yang, J. Jing, W. Li, Y. Zhu, Electron donor-acceptor interface of TPPS/PDI boosting charge transfer for efficient photocatalytic hydrogen evolution, Adv. Sci. 9 (2022) 2201134.

[11] J. Jing, J. Yang, Z. Zhang, Y. Zhu, Supramolecular zinc porphyrin photocatalyst with strong reduction ability and robust built-in electric field for highly efficient hydrogen production, Adv. Energy Mater. 11 (2021). Article 2101392.

[12] J. Yang, J. Jing, Y. Zhu, A full-spectrum porphyrin-fullerene D-A supramolecular photocatalyst with giant built-in electric field for efficient hydrogen production, Adv. Mater. 33 (2021) 2101026.

[13] J. Jing, J. Yang, W. Li, Z. Wu, Y. Zhu, Construction of interfacial electric field via dual-porphyrin heterostructure boosting photocatalytic hydrogen evolution, Adv. Mater. 34 (2022) 2106807.

[14] X. Li, X. Wen, J. Lang, Y. Wei, J. Miao, X. Zhang, B. Zhou, M. Long, P. Alvarez, L. Zhang, CoN_1O_2 single-atom catalyst for efficient peroxymonosulfate activation and selective cobalt(IV)=O generation, Angew. Chem. Int. Ed. 62 (2023) e202303267.

[15] Z. Luo, X. Chen, Y. Hu, X. Chen, W. Lin, X. Wu, X. Wang, Side-chain molecular engineering of triazole-based donor-acceptor polymeric photocatalysts with strong electron push-pull interactions, Angew. Chem. Int. Ed. 62 (2023) e202304875.

[16] H. Cheng, H. Lv, J. Cheng, L. Wang, X. Wu, H. Xu, Rational design of covalent heptazine frameworks with spatially separated redox centers for high-efficiency photocatalytic hydrogen peroxide production, Adv. Mater. 34 (2021) 2107480.

[17] Y. Wu, X. Mao, M. Zhang, X. Zhao, R. Xue, S. Di, W. Huang, L. Wang, Y. Li, Y. Li, 2D molecular sheets of hydrogen-bonded organic frameworks for ultrastable sodium-ion storage, Adv. Mater. 33 (2021) 2106079.

[18] P. Han, F. Liu, Y. Zhang, Y. Wang, G. Qin, L. Hou, C. Yuan, Organic-inorganic hybridization engineering of polyperylenediimide cathodes for efficient potassium storage, Angew. Chem. Int. Ed. 60 (2021) 23596–23601.

[19] Y. Guo, Q. Zhou, J. Nan, W. Shi, F. Cui, Y. Zhu, Perylenetetracarboxylic acid nanosheets with internal electric fields and anisotropic charge migration for photocatalytic hydrogen evolution, Nat. Commun. 13 (2022) 2067.

[20] G. Xing, T. Yan, S. Das, T. Ben, S. Qiu, Synthesis of crystalline porous organic salts with high proton conductivity, Angew. Chem. Int. Ed. 57 (2018) 5345–5349.

[21] W. Li, S. Wu, H. Zhang, X. Zhang, J. Zhuang, C. Hu, Y. Liu, B. Lei, L. Ma, X. Wang, Enhanced biological photosynthetic efficiency using light-harvesting engineering with dual-emissive carbon dots, Adv. Funct. Mater. 28 (2018) 1804004.

[22] E. Ravera, S. Ciambellotti, L. Cerofolini, T. Martelli, T. Kozyreva, C. Bernacchioni, S. Giuntini, M. Fragai, P. Turano, C. Luchinat, Solid-state NMR of PEGylated proteins, Angew. Chem. Int. Ed. 55 (2016) 2446–2449.

[23] H. Duan, P. Lyu, J. Liu, Y. Zhao, Y. Xu, Semiconducting crystalline two-dimensional polyimide nanosheets with superior sodium storage properties, ACS Nano 13 (2019) 2473–2480.

[24] Y. Tian, W. Que, Y. Luo, C. Yang, X. Yin, L.B. Kong, Surface nitrogen-modified 2D titanium carbide (MXene) with high energy density for aqueous supercapacitor applications, J. Mater. Chem. A 7 (2019) 5416–5425.

[25] F. Han, S. Luo, L. Xie, J. Zhu, W. Wei, X. Chen, F. Liu, W. Chen, J. Zhao, L. Dong, K. Yu, X. Zeng, F. Rao, L. Wang, Y. Huang, Boosting the yield of mXene 2D sheets via a facile hydrothermal-assisted intercalation, ACS Appl. Mater. Interfaces 11 (2019) 8443–8452.

[26] K.S. Park, K.S. Lee, J. Baek, L. Lee, B.H. Son, Y.E. KooLee, Y.H. Ahn, W.I. Park, Y. Kang, M.M. Sung, Observation of charge separation and space-charge region in single-crystal P3HT/C_{60} heterojunction nanowires, Angew. Chem. Int. Ed. 128 (2016) 10429–10433.

[27] J.M. Park, K.-I. Hong, H. Lee, W.-D. Jang, Bioinspired applications of porphyrin derivatives, Acc. Chem. Res. 54 (2021) 2249–2260.

[28] S. Hayakawa, K. Matsuo, H. Yamada, N. Fukui, H. Shinokubo, Dinaphthothiepine bisimide and its sulfoxide: soluble precursors for perylene bisimide, J. Am. Chem. Soc. 142 (2020) 11663–11668.

[29] Y.I.H. Chao, J.-F. Jheng, J.-S. Wu, K.-Y. Wu, H.-H. Peng, M.-C. Tsai, C.-L. Wang, Y.-N. Hsiao, C.-L. Wang, C.-Y. Lin, C.-S. Hsu, Porphyrin-Incorporated 2D D–A Polymers with Over 8.5% polymer solar cell efficiency, Adv. Mater. 26 (2014) 5205–5210.

[30] Zhang, C. Li, F. Yang, J. Zhang, Z. Wang, Z. Wei, W. Li, An electron acceptor with porphyrin and perylene bisimides for efficient non-fullerene solar cells, Angew. Chem. Int. Ed. 129 (2017) 2738–2742.

[31] Z. Chen, V. Stepanenko, V. Dehm, P. Prins, L.D.A. Siebbeles, J. Seibt, P. Marquetand, V. Engel, F. Würthner, Photoluminescence and conductivity of self-assembled π–π stacks of perylene bisimide dyes, Chem. Eur. J. 13 (2007) 436–449.

[32] Y. Wei, J. Zhang, Q. Zheng, J. Miao, P. Alvarez, M. Long, Quantification of photocatalytically-generated hydrogen peroxide in the presence of organic electron donors: interference and reliability considerations, Chemosphere 279 (2021) 130556.

[33] K. Wang, C.-J. Zheng, W. Liu, K. Liang, Y.-Z. Shi, S.-L. Tao, C.-S. Lee, X.-M. Ou, X.-H. Zhang, Avoiding energy loss on TADF emitters: controlling the dual conformations of D-A structure molecules based on the pseudoplanar segments, Adv. Mater. 29 (2017) 1701476.

[34] K.-K. Takashi, M. Masayuki, T. Hideyuki, H. Yoshihiro, N. Taneo, Photoreflectance characterization of built-in potential in MBE-produced as-grown GaAs surface, Proc. SPIE (1990) 56–65.

[35] G. Morello, F. Della Sala, L. Carbone, L. Manna, G. Maruccio, R. Cingolani, M. De Giorgi, Intrinsic optical nonlinearity in colloidal seeded grown CdSe/CdS nanostructures: photoinduced screening of the internal electric field, Phys. Rev. B 78 (2008) 195313.

[36] F. Le Formal, K. Sivula, M. Grätzel, The transient photocurrent and photovoltage behavior of a hematite photoanode under working conditions and the influence of surface treatments, J. Phys. Chem. C. 116 (2012) 26707–26720.

[37] X. Zhang, J. Zhang, J. Miao, X. Wen, C. Chen, B. Zhou, M. Long, Keto-enamine-based covalent organic framework with controllable anthraquinone moieties for superior H₂O₂ photosynthesis from O₂ and water, Chem. Eng. J. 466 (2023) 143085.

[38] J. Zhang, J. Lang, Y. Wei, Q. Zheng, L. Liu, Y. Hu, B. Zhou, C. Yuan, M. Long, Efficient photocatalytic H₂O₂ production from oxygen and pure water over graphitic carbon nitride decorated by oxidative red phosphorus, Appl. Catal. B 298 (2021) 120522.

[39] G.Z. Wang, Q.L. Sun, Y.Y. Liu, B.B. Huang, Y. Dai, X.Y. Zhang, X.Y. Qin, A Bismuth-based metal-organic framework as an efficient visible-light-driven photocatalyst Chem, Eur. J. 21 (2015) 2364–2367.

[40] L. Chen, C. Chen, Z. Yang, S. Li, C. Chu, B. Chen, Simultaneously tuning band structure and oxygen reduction pathway toward high-efficient photocatalytic hydrogen peroxide production using cyano-rich graphitic carbon nitride, Adv. Funct. Mater. 31 (2021) 2105731.

[41] Z.J. Zhang, X.J. Chen, H.J. Zhang, W.X. Liu, W. Zhu, Y.F. Zhu, A Highly crystalline perylene imide polymer with the robust built-in electric field for efficient photocatalytic water oxidation, Adv. Mater. 32 (2020) 1907746.

[42] Q. Zhi, W. Liu, R. Jiang, X. Zhan, Y. Jin, X. Chen, X. Yang, K. Wang, W. Cao, D. Qi, J. Jiang, Piperazine-linked metalphthalocyanine frameworks for highly efficient visible-light-driven H₂O₂, Photosynth., J. Am. Chem. Soc. 144 (2022) 21328–21336.

[43] L. Chen, L. Wang, Y. Wan, Y. Zhang, Z. Qi, X. Wu, H. Xu, Acetylene and diacetylene functionalized covalent triazine frameworks as metal-free photocatalysts for hydrogen peroxide production: a new two-electron water oxidation pathway, Adv. Mater. 32 (2020) 1904433.

[44] H. Koshima, K. Takechi, H. Uchimoto, M. Shiro, D. Hashizume, Photomechanical bending of salicylideneaniline crystals, ChemComm 47 (2011) 11423–11425.

[45] H. Wang, C. Yang, F. Chen, G. Zheng, Q. Han, A crystalline partially fluorinated triazine covalent organic framework for efficient photosynthesis of hydrogen peroxide, Angew. Chem. Int. Ed. 61 (2022) e202202328.

[46] Y. Shiraishi, S. Kanazawa, Y. Sugano, D. Tsukamoto, H. Sakamoto, S. Ichikawa, T. Hirai, Highly selective production of hydrogen peroxide on graphitic carbon nitride (g-C₃N₄) photocatalyst activated by visible light, ACS Catal. 4 (2014) 774–780.

[47] P. Zhang, Y. Tong, Y. Liu, J.J.M. Vequizo, H. Sun, C. Yang, A. Yamakata, F. Fan, W. Lin, X. Wang, W. Choi, Heteroatom dopants promote two-electron O₂ reduction for photocatalytic production of H₂O₂ on polymeric carbon nitride, Angew. Chem. Int. Ed. 59 (2020) 16209–16217.

[48] Z. Wei, M.L. Liu, Z.J. Zhang, W.Q. Yao, H.W. Tan, Y.F. Zhu, Efficient visible-light-driven selective oxygen reduction to hydrogen peroxide by oxygen-enriched graphitic carbon nitride polymers, Energy Environ. Sci. 11 (2018) 2581–2589.